crystals

MDPI

Article

Green Synthesis of Nanomagnetic Copper and Cobalt Ferrites Using Corchorus Olitorius

Nada S. Al-Kadhi [1], Ghadah M. Al-Senani [1], Rasmiah S. Almufarij [1], Omar H. Abd-Elkader [2,*] and Nasrallah M. Deraz [3]

[1] Department of Chemistry, College of Science, Princess Nourah Bint Abdulrahman University, P.O. Box 84428, Riyadh 11671, Saudi Arabia; nsalkadhi@pnu.edu.sa (N.S.A.-K.); gmalsnany@pnu.edu.sa (G.M.A.-S.); rsmufrrig@pnu.edu.sa (R.S.A.)
[2] Physics and Astronomy Department, Science College, King Saud University, P.O. Box 2455, Riyadh 11451, Saudi Arabia
[3] Physical Chemistry Department, National Research Centre, P.O. Box 21111, Giza 12622, Egypt; nm.mahmoud@nrc.sci.eg
* Correspondence: omabdelkader7@ksu.edu.sa

Abstract: This study aims to develop a self-combustion method for use in the preparation of copper and cobalt ferrites. This development was based on the full use of dry leaves of Corchorus olitorius plant in order to stimulate the preparation of the studied ferrites by making full use of the small amount of carbon produced from the combustion process. The fabrication of $CuFe_2O_4$ and $CoFe_2O_4$ with spinel-type structures and the Fd3m space group is confirmed by XRD and FTIR investigations. Two major vibration bands occur laterally at 400 cm^{-1} and 600 cm^{-1}. We were able to understand the existence of two stages through the thermal behavior based on TG-DTG analysis for the materials under investigation. The first is from room temperature to 600 °C, which indicates the formation of reacting oxides with Co or Cu ferrites, while the second is from 600–1000 °C, which indicates the growth in the ferrite fabrication. The surface morphological analyses (SEM/EDS and TEM) display formation of homogeneous and nanosized particles. The surface properties of the samples containing $CoFe_2O_4$ are superior compared to those of the samples not containing $CuFe_2O_4$. Every sample under investigation displays type-IV-based isotherms with a type-H3 hysteresis loop. The VSM approach was used to evaluate the magnetic characteristics of Cu and Co ferrites. Copper ferrites have a magnetization of 15.77 emu/g, and cobalt ferrites have a magnetization of 19.14 emu/g. Moreover, the squareness (0.263) and coercivity (716.15 G) of cobalt ferrite are higher than those of copper ferrite.

Keywords: XRD; FTIR; SEM/EDS; TEM; S_{BET}; $CuFe_2O_4$; $CoFe_2O_4$; magnetization

check for updates

Citation: Al-Kadhi, N.S.; Al-Senani, G.M.; Almufarij, R.S.; Abd-Elkader, O.H.; Deraz, N.M. Green Synthesis of Nanomagnetic Copper and Cobalt Ferrites Using Corchorus Olitorius. *Crystals* **2023**, *13*, 758. https://doi.org/10.3390/cryst13050758

Academic Editor: Jan Macutkevic

Received: 31 March 2023
Revised: 24 April 2023
Accepted: 25 April 2023
Published: 3 May 2023

Copyright: © 2023 by the authors. Licensee MDPI, Basel, Switzerland. This article is an open access article distributed under the terms and conditions of the Creative Commons Attribution (CC BY) license (https://creativecommons.org/licenses/by/4.0/).

1. Introduction

Many scientific research groups around the world have been interested in determining the relationship between the preparation of ceramic nanostructured materials such as ferrites and their different physical and chemical properties. Advanced studies were and still are working to improve the methods of preparing different ferrites, which are highly required due to the impact of this on all of their multiple properties. There are many methods to prepare different ferrites depending on specific strategies that seek to produce them via an economical route, based on reducing the consumption of time, effort, and raw materials and reaching the highest productivity and best properties. With the current technological advances, various series of routes have been reported for the fabrication of ferrite materials, including the processes of co-precipitation, hydrothermal method, solid-state reaction, sol-gel method, mechanical milling and self-combustion [1–12].

In this regard, the self -combustion method has been used to prepare various ferrites due to its ease, simplicity, low cost, short time of synthesis, and high purity of product [6–8]. In this method, choosing the suitable reducer is very important because it behaves as

a reducing and complicating agent. Among the most commonly used fuels are urea, glycine, and egg white [6,13–16]. Indeed, biosynthesis approaches are widely accepted and selected because they have various advantages such as eco-friendliness, economy, and sustainability with an excellent yield [17]. In this context, our present study has adapted a Corchorus olitorius mediated combustion method for synthesis of both copper and cobalt ferrite nanoparticles.

Deraz research group took the lead in conducting a comparative study between the use of the dried leaves of Corchorus olitorius in the combustion process and the use of its extract to prepare Ni/NiO nanocomposite. This group found that the use of the dried leaves of Corchorus olitorius, not its extract, is the best, which led to an enhancement in the formation of nickel metal, including the as-prepared composite [18]. These results motivated this group to prepare both copper and cobalt ferrites using the dried leaves of Corchorus olitorius in this study.

Cobalt ferrite ($CoFe_2O_4$) is a semi-hard matter because it can be considered as falling between soft and hard magnetic materials according to its coercivity, while copper ferrite ($CuFe_2O_4$) is a soft magnetic material due to relativity low coercivity [19–21]. Some authors reported that the coercivity of $CoFe_2O_4$ nanoparticles is usually low, e.g., only about 4.3 G and 7.6 G [22,23]. On the other hand, other authors observed a high coercivity value for cobalt ferrite, up to 1876 G, with high magnetization (78 emu/g) [24]. In addition, $CuFe_2O_4$ synthesized by urea-assisted combustion route possessed a saturation magnetization of 5.47 emu/g and an intrinsic coercive force of 241.98 G [25]. These different results confirm that the magnetic behavior of both copper and cobalt ferrites is related to the method of their preparation.

Moreover, $CuFe_2O_4$ and $CoFe_2O_4$ have an inverse spinel-type structure, including Cu^{2+} and Co^{2+} ions at A-site and Fe^{3+} at both A- and B-sites [6,13–16]. Due to their chemical stability, mechanical hardness, and distinctive optical, electrical, magnetic, and semiconducting capabilities, $CuFe_2O_4$ and $CoFe_2O_4$ based nanoparticles are particularly promising materials. These ferrites, like the other spinel ferrites, are particularly efficient materials because $CuFe_2O_4$ and $CoFe_2O_4$ can be employed in a variety of applications, including magnetic drug delivery systems, multi-layer chip inductors, magnetic separation, high-density storage media, ferromagnetic fluids, catalysts, solar hydrogen production, gas sensors, and magnetic resonance tomography [26–28]. In addition, the phase transition of $CuFe_2O_4$ at various temperatures from cubic to tetragonal phase depends on John–Teller (J-T) distortion of Cu^{2+} ions and inversion degree, which is the fraction of the iron atoms occupying tetrahedral sites [28–30]. The J-T effect plays a significant role in the loss of crystal symmetry as results in a phase transition. By altering the synthesis process and heat treatment method, this effect can be reduced to a minimum [31]. Generally, the inversion degree of spinel-structure-based ferrites mainly depends on the method of synthesis and their thermal history [32,33]. Some researchers obtained inversion degrees of 0.77 and 0.70 for Co ferrites prepared using the solvothermal method with particle sizes of 100 and 15 nm, respectively [34]. Inversion orders of 0.72 and 0.70 were observed by other researchers for Co ferrite prepared with size of 6 nm using the thermal decomposition route [35,36].

In this work, direct interaction between the metal nitrates and dry leaves of Corchorus olitorius powders resulted in the effective synthesis of nanocrystalline $CuFe_2O_4$ and $CoFe_2O_4$. The thermal, structural, surface, morphological, and magnetic properties of the as-synthesized ferrites were investigated. This study determined how a heat treatment at 700 °C for two hours would affect the various properties of the solids as they were manufactured.

2. Materials and Methods

2.1. Materials

The Sigma-Aldrich Company (Darmstadt, Taufkirchen, Germany) provided the chemical ingredients used, which were $Cu(NO_3)_2{\cdot}3H_2O$, $Co(NO_3)_2{\cdot}6H_2O$, and $Fe(NO_3)_3{\cdot}9H_2O$. No additional processing was necessary for these reagents, which were used quantitatively.

From the agricultural environment of Egypt, dry leaves of Corchorus olitorius are used to make powders.

2.2. Preparation Method

The dry leaves of Corchorus olitorius powders were utilized as fuel in the combustion-process-based preparation method to create two samples (S1 and S2) containing $CuFe_2O_4$ and $CoFe_2O_4$, respectively, with a focus on the stoichiometric ratio of Fe/M = 2 (M = Cu and Co). These samples were created in a crucible by thoroughly mixing an equimolar mixture of ferric metal nitrates hydrate with 0.5 g of powdered dry Corchorus olitorius leaves. The resultant materials were heated at 60 °C to remove the water and increase viscosity. They were heated for 15 min at a temperature of 300 °C after 120 °C to produce the precursor gel. Something like a spark appeared in one of the crucible's sides and spread quickly all across the material in its present state, which gave the impression of an illuminating flame. A significant amount of foam had already started forming. A substance that was simultaneously dense and fluffy was the final outcome. Furthermore, 2 more samples (S3 and S4) were created by burning various portions of the S1 and S2 samples, respectively, at 700 °C for 2 h.

2.3. Characterization Systems

A computerized Shimadzu thermal analyzer (Shimadzu, Osaka, Osaka, TGA 60 Japan) was used to conduct the thermogravimetry (TG) and differential derivative thermogravimetry analysis (DTG). With air flowing at a rate of 30 mL per minute and heating rate of 10 °C per minute, the studied solids were analyzed. Certain weights of the as-prepared samples were chosen in order to minimize the impact of sample weight caused by peak shape and temperature. Alumina (α-Al_2O_3) has also been employed as the reference source.

The structural characteristics of several nanoparticles were determined using an X-ray diffraction-based BRUKER D8 advance diffractometer (Karlsruhe, Germany). Cu Kα radiation was used to run the patterns at 40 kV, 40 mA, and a scanning speed of 2° per minute. According to calculations using the Scherrer equation and X-ray diffraction line broadening, at the plane (311) Equations (1)–(3) have been utilized to determine the mean crystallite size (d), strain (ε), and dislocation density (δ) of copper and cobalt ferrites present in the examined product [37]:

$$d = B\lambda \div \beta \cos\theta \quad (1)$$

$$\delta = 1 \div d^2 \quad (2)$$

$$\varepsilon = \beta \cos\theta \div 4 \quad (3)$$

In this formula, d is the average crystallite size of the phase being investigated, B is the Scherrer constant (0.89), λ is the wavelength of the used X-ray beam, β is the full-width half-maximum (FWHM) of diffraction, and θ is the Bragg's angle.

The Fourier transmission infrared spectra (FTIR) of various materials in the region of 4000–400 cm^{-1} could be evaluated using a Perkin-Elmer Spectrophotometer (type 1430). A total of 200 mg of vacuum-dried IR-grade KBr was combined with 2 mg of each solid sample. Once the mixture had been treated in a vibrating ball mill for 3 min, it was dispersed using a steel die with a 13 mm diameter. The double-grating FTIR spectrophotometer holder was inserted with the same disks.

Through the application of the JEOL JAX-840A and JEOL Model 1230 (both from JEOL, Tokyo, Japan), respectively, scanning electron microscopy (SEM) images and transmittance electron micrograph (TEM) images of the solids as prepared were captured. The samples were first dissolved in ethanol and then subjected to a brief treatment with ultrasonography in order to distribute individual particles over mount setup and Cu grids.

With a Delta Kevex device connected to an electron microscope, the JAX-840A Series, energy-dispersive X-ray analysis (EDS with Mapping) was successfully performed (JEOL, Tokyo, Japan). The following settings were utilized: 20 kV accelerating voltage, 120 s of accumulation time, and 6 m of window width. The Asa technique, Zaf correction, and Gaussian approximation were used to determine the surface molar composition.

The Gemini VII 2390 V1.03 series of surface area analyzers from Micrometrics (Micrometrics, Alpharetta, GA, USA) were used to calculate surface area (S_{BET}), total pore volume (V_P), monolayer adsorption volume (V_m), and mean pore radius ($\hat{r}$) of representative samples from nitrogen adsorption isotherms at 77 K. Before the measurements, each sample was out-gassed for 2 h at 200 °C at a lower pressure of 10^{-5} Torr.

At a maximum applied field of 20 kG, the magnetic characteristics of the solids as manufactured were ascertained using a vibrating sample magnetometer (VSM; 9600–1 LDJ, Lowell, MA, USA).

3. Results

3.1. TG/DTG Analysis

As seen in Figure 1, TG/DTG analysis was utilized to examine the thermal behavior of the S1 and S2 solids. Analysis of this graph revealed the following: (i) Dehydration, breakdown, and solid-state reaction were among the processes that occurred as the heat treatment temperature was raised from room temperature to 1000 °C. (ii) The DTG curves of the S1 and S2 specimens were made up entirely of 3 exothermic peaks at 27.2, 225.5, and 675.5 °C, which represented the release of moisture, hydration of water, and elimination of carbon as a result of combustion of the dry leaves of Corchorus olitorius, respectively. (iii) The TG curve of the S2 specimen shows weight losses of 8.1% and 5.2% in the temperature ranges of 25–275 °C and 275–1000 °C, respectively. The first weight loss indicates the course of the dehydration process. Moreover, the second weight loss is related to the conversion process of Co and Fe oxides to $CoFe_2O_4$ crystallites with subsequent elimination of the residual of carbon. (iii) The TG curve of the S1 specimen shows weight losses of 8.1% and 5.2% in the temperature ranges of 25–580 °C and 580–1000 °C, respectively. The 8.1% weight loss indicates the course of the dehydration process and the partially solid-state reaction between Cu and Fe oxides yielding Cu ferrite. Meanwhile, the 5.2% weight loss is related to the complete conversion of these oxides to $CuFe_2O_4$ crystallites with subsequent elimination of the residual of carbon.

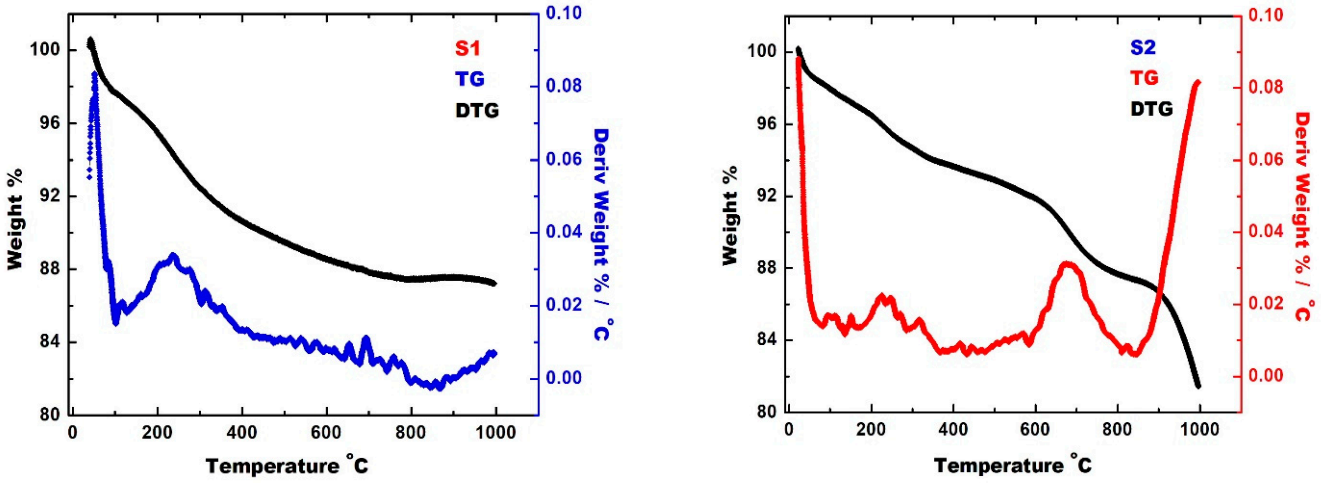


Figure 1. TG and DTG curves of the S1 and S2 samples.

3.2. XRD Analysis

The as-prepared $CuFe_2O_4$ and $CoFe_2O_4$ nanoparticles can be estimated using the XRD technique. The patterns of XRD from this technique for the as-prepared solids are shown in Figure 2. Examining XRD patterns for the S1 specimen, we found the following diffraction peaks with the corresponding planes: (220), (311), (400), (511), and (440), which were located at 2θ = 30.26°, 35.62°, 43.24°, 57.19°, and 62.76°, respectively. The diffraction of the cubic spinel structure with the Fd3m space group for $CuFe_2O_4$ is compatible with these planes (PDF no. 35–0425). The XRD pattern of the S3 sample and Table 1 demonstrate that the heat treatment of this sample at 700 °C caused these peaks to shift somewhat in position and grow slightly in height. The S2 specimen exhibits additional diffraction peaks at 2 = 18.72°, 30.1°, 35.46°, 44°, and 62.5°, respectively, at the following planes: (111), (220), (311), (400), and (440). These peaks agree with the $CoFe_2O_4$ (PDF no. 22–1086) standard diffraction for the cubic spinel structure and Fd3m space group. According to the XRD pattern of the S4 sample and Table 1, the calcination of this sample at 700 °C caused these peaks' positions to shift somewhat and their heights to significantly rise. The miller indices, two thetas (2θ observed and calculated), and the differences between the values of two thetas for the S1, S2, S3, and S4 samples are tabulated in Table 1.

Table 1. Miller indices for $CuFe_2O_4$ in the S1 and S3 samples and for $CoFe_2O_4$ in the S2 and S4 samples.

h	k	l	S1 ($CuFe_2O_4$)			S3 ($CuFe_2O_4$ Δ700)		S2 ($CoFe_2O_4$)			S4 ($CoFe_2O_4$ Δ700)	
			2θ Calc.	2θ Obs.	Diff.	2θ Obs.	Diff.	2θ Calc.	2θ Obs.	Diff.	2θ Obs.	Diff.
1	1	1	18.39	18.3735	0.0165	18.3678	0.0222	18.39	18.4051	−0.0151	18.3924	−0.0624
0	2	2	30.28	30.2247	0.0553	30.215	0.065	30.28	30.2774	0.0026	30.2562	0.3938
3	1	1	35.45	35.6020	−0.1520	35.5906	0.2894	35.45	35.6648	−0.2148	35.6395	−0.0495
2	2	2	37.30	37.2419	0.0581	37.2299	0.0701	37.37	37.3077	0.0623	37.2812	0.0888
0	0	4	43.32	43.2713	0.0487	43.2571	0.0629	43.32	43.3488	−0.0288	43.3176	0.0024
3	1	3	47.54	47.3796	0.1604	47.3639	0.1161	47.54	47.4653	0.0747	47.4308	0.1092
4	2	2	53.88	53.6885	0.1915	53.6705	0.0195	53.88	53.7874	0.0926	53.7476	0.3424
3	3	3	57.08	57.2349	−0.1549	57.2154	−0.1354	57.40	57.3415	0.0585	57.2985	0.1015
0	4	4	63.03	62.8557	0.1743	62.8339	0.0361	63.03	62.9751	0.0549	62.927	−0.457
5	1	3	66.17	66.0929	0.0771	66.0697	−0.0297	66.17	66.2200	−0.0500	66.1688	−0.1988
2	4	4	67.04	67.1536	−0.1136	67.1300	−0.0900	67.38	67.2833	0.0967	67.2311	0.1489
2	0	6	71.35	71.3195	0.0305	71.2939	0.0561	71.35	71.4597	−0.1097	71.4032	−0.0532
5	3	3	74.26	74.3766	−0.1166	74.3496	−0.0896	74.42	74.5249	−0.1049	74.4651	−0.0451
2	2	6	75.27	75.3852	−0.1152	75.3576	−0.0876	75.64	75.5362	0.1038	75.4753	−0.0053
4	4	4	79.81	79.3768	0.4332	79.3472	0.0528	-	-	-	-	-

By computing the lattice constant (a), unit cell volume (V), and X-ray density (Dx) based on the XRD results, some characteristics of the crystal structure for the corresponding ferrites in the S1, S2, S3, and S4 samples were identified. Other structural parameters, such as strain (ε), dislocation density (δ), the distance between magnetic ions (L_A and L_B), ionic radii (r_A, r_B), and bond lengths (A-O and B-O) on tetrahedral (A) and octahedral (B) sites, were also computed for the as-synthesized ferrites by making the best use of the XRD results. Table 2 contains the determined values of all the prior formal factors. Using this chart as a guide, the following was discovered: Cu and Co ferrites' strain and dislocation density decreased as a result of the heat treatment at 700 °C, which also caused a rise in the crystallite size of the materials. (ii) By heating cobalt ferrite to 700 °C, the values of a, V, L_A, L_B, r_A, r_B, A-O, and B-O drop as the D_x value increases.

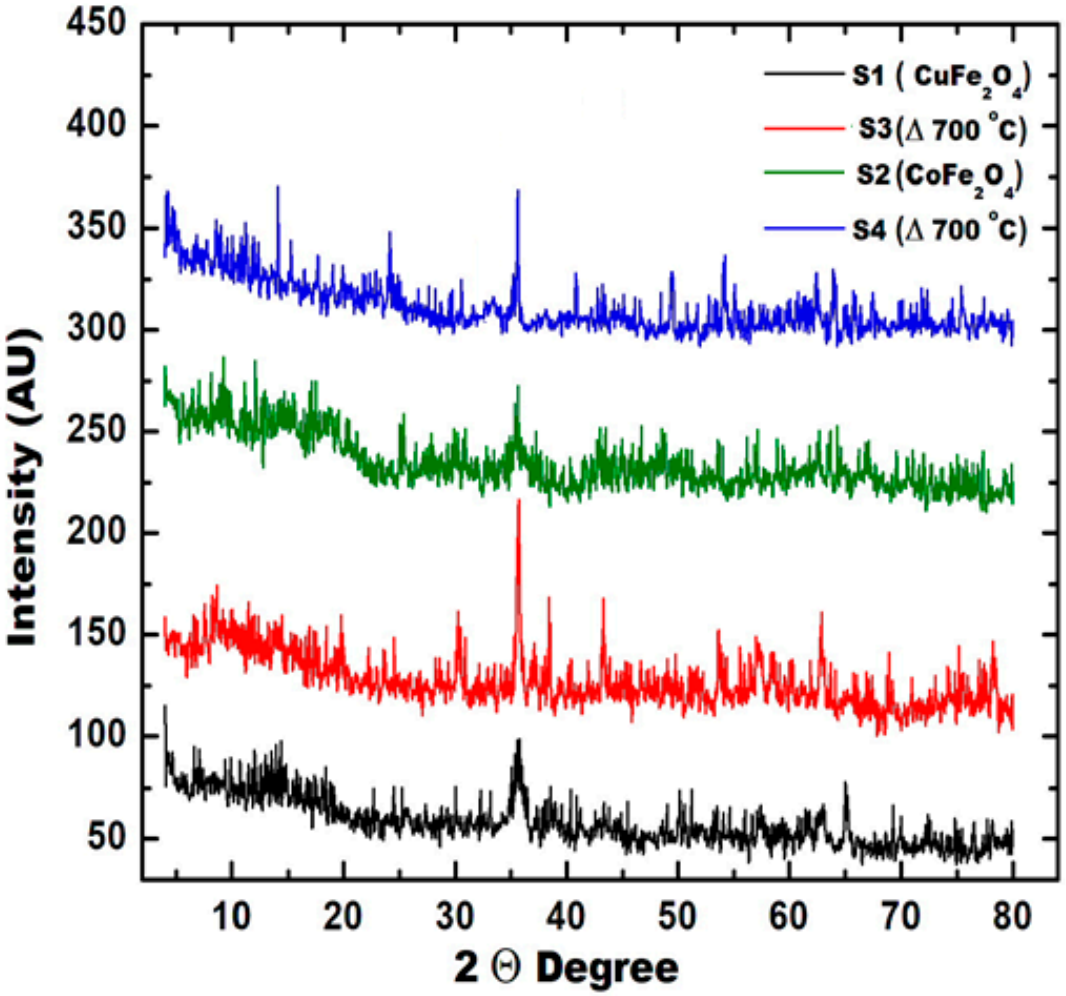


Figure 2. XRD patterns of S1, S2, S3, and S4 specimens.

Table 2. Lattice parameters for $CuFe_2O_4$ in the S1 and S3 samples and for $CoFe_2O_4$ in the S2 and S4 samples.

Parameters	S1	S2	S3	S4
a, nm	0.83497	0.83552	0.83639	0.83661
α	90.00	90.00	90.00	90.00
β	90.00	90.00	90.00	90.00
γ	90.00	90.00	90.00	90.00
Volume (V), nm^3	0.58212	0.58330	0.58510	0.58560
Crystallite Size (d), nm	18.840	54.110	17.902	60.317
D_x, g/cm^3	5.4577	5.3418	5.4299	5.3208
L_A, nm	0.3615	0.3618	0.3622	0.3623
L_B, nm	0.2950	0.2953	0.2956	0.2957
A-O, nm	0.1909	0.1910	0.1912	0.1913
B-O, nm	0.2154	0.2157	0.2158	0.2159
r_A, nm	0.0589	0.0590	0.0592	0.0593
r_B, nm	0.0834	0.0837	0.0838	0.0839
δ, Lines/nm	2.82×10^{-3}	3.42×10^{-4}	3.12×10^{-3}	2.75×10^{-4}
ε	1.84×10^{-3}	6.41×10^{-4}	1.94×10^{-3}	1.81×10^{-4}

3.3. FTIR Analysis

FTIR analysis can be used to identify the S1, S2, S3, and S4 specimens' chemical functional groups. Waldron's report must be taken into account, since the studied samples contain various ferrites [38]. This report, which many researchers took into consideration, serves as the primary source for confirming the production of ferrites. The two fundamental vibration modes, which are connected to the cation distribution at the tetrahedral (A-) and octahedral (B-) sites, respectively, emerged in the FTIR spectra of the spinel ferrites around 600 cm^{-1} and 400 cm^{-1}, as described in this analysis. In this study, Figure 3 shows the FTIR spectra of the S1, S2, S3, and S4 samples in the 4000–400 cm^{-1} region at room temperature. Through this figure, we notice the following: (i) The S1, S2, S3, and S4 samples exhibited two main absorption bands (v_1 and v_2) at 556–530 cm^{-1} and 413–407 cm^{-1}. The presence of these bands is consistent with Waldron's report and confirms the formation of spinel-type ferrites. These bands came as a result of the metal–oxygen (M–O) bond-stretching vibrations. In other words, these bands are due to Fe-O, Co-O, and Cu-O vibrations at both A- and B-sites according to the kind of spinel ferrite studied. Based on our previous works, Cu, and Co cations prefer to be in B-site, while Fe cations can be distributed between A- and B-sites, leading to formation of inverse spinel ferrites [7,8]. (ii) Waldron pointed out that it is possible that the two fundamental vibration modes may be accompanied by some shoulders, or they may be splitting. In this context, the authors observed small shoulders (v_1*) and small subsidiary bands due to splitting of absorption band (v_2*) in all samples located at 690–660 cm^{-1} and 418–416 cm^{-1}, respectively. They assumed the emergence of v_1* is due to the vibration of divalent cations for copper or cobalt [7,8,39,40]. The presence of v_2* may be due to John–Teller ions of Fe^{2+} oxygen complexes in an octahedral site, which causes the splitting in an absorption band. This finding confirms the presence of local lattice deformation with subsequent reduction in the symmetry of crystals. These observations, therefore, confirm that all prepared ferrites have random spinel structure. (iii) The stretching and bending vibrations of the hydroxyl groups (O-H), which adsorbed water molecules on the surface of the S1, S2, S3, and S4 samples, may also be responsible for the bands at 3248–2905 cm^{-1} and 1628–1550 cm^{-1}. (iv) The FTIR curves of the S1 and S2 specimens were included on bands in the range of 1356–1348 cm^{-1} associated with the stretching vibrations of hydrogen carbon and hydroxyl carbon (C-OH and C-H), depending on the presence of carbon traces that arose from an internal combustion process of Corchorus olitorius powder [39]. Instead, after these samples are calcined at 700 °C, the bands associated with the vibrations of both C-OH and C-H vanish in the case of S3 and S4 specimens. (v) The heat treatment of the as-prepared samples at 700 °C caused all the bands' locations to change and their intensities to rise as a result.

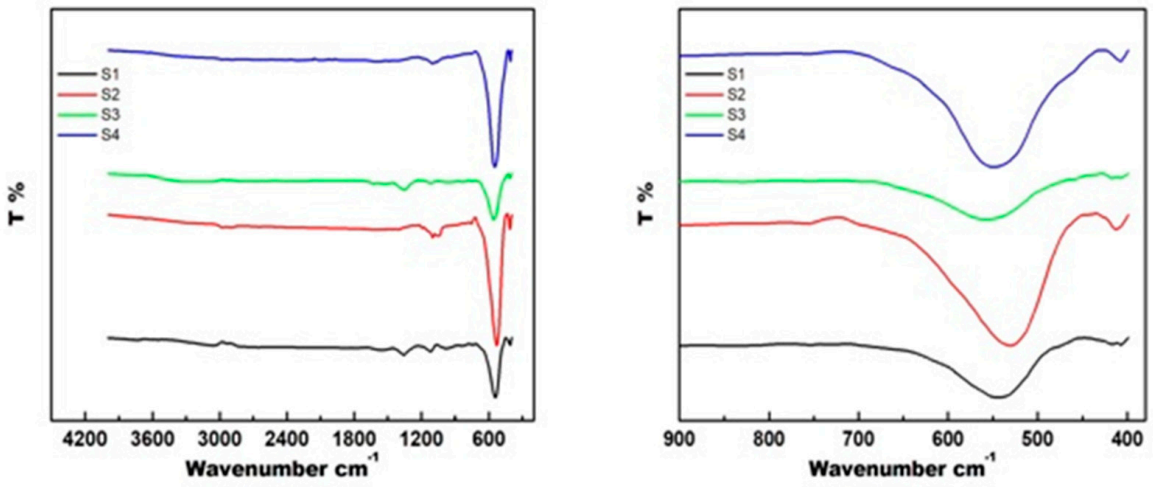


Figure 3. FTIR of S1, S2, S3, and S4 specimens.

3.4. Morphological Studies

The surface morphology of the as-prepared solids is studied to explore the shape, nature, and size of their particles. In addition, the morphological study explains much of the influence of the size and nature of the particles on their structural, surface, and magnetic properties. Among the analyses that helped in the morphological studies were SEM, EDS mapping, and TEM techniques. Figure 4 contains the SEM analysis of the S1 and S2 samples and demonstrates that these materials have a brittle and spongy structure with pores and spaces. This graphic makes it obvious that the S2 particles are smaller than the S1 particles, which is in line with the XRD data. The surface morphology of the S1 and S2 specimens clearly shows the presence of some aggregates.

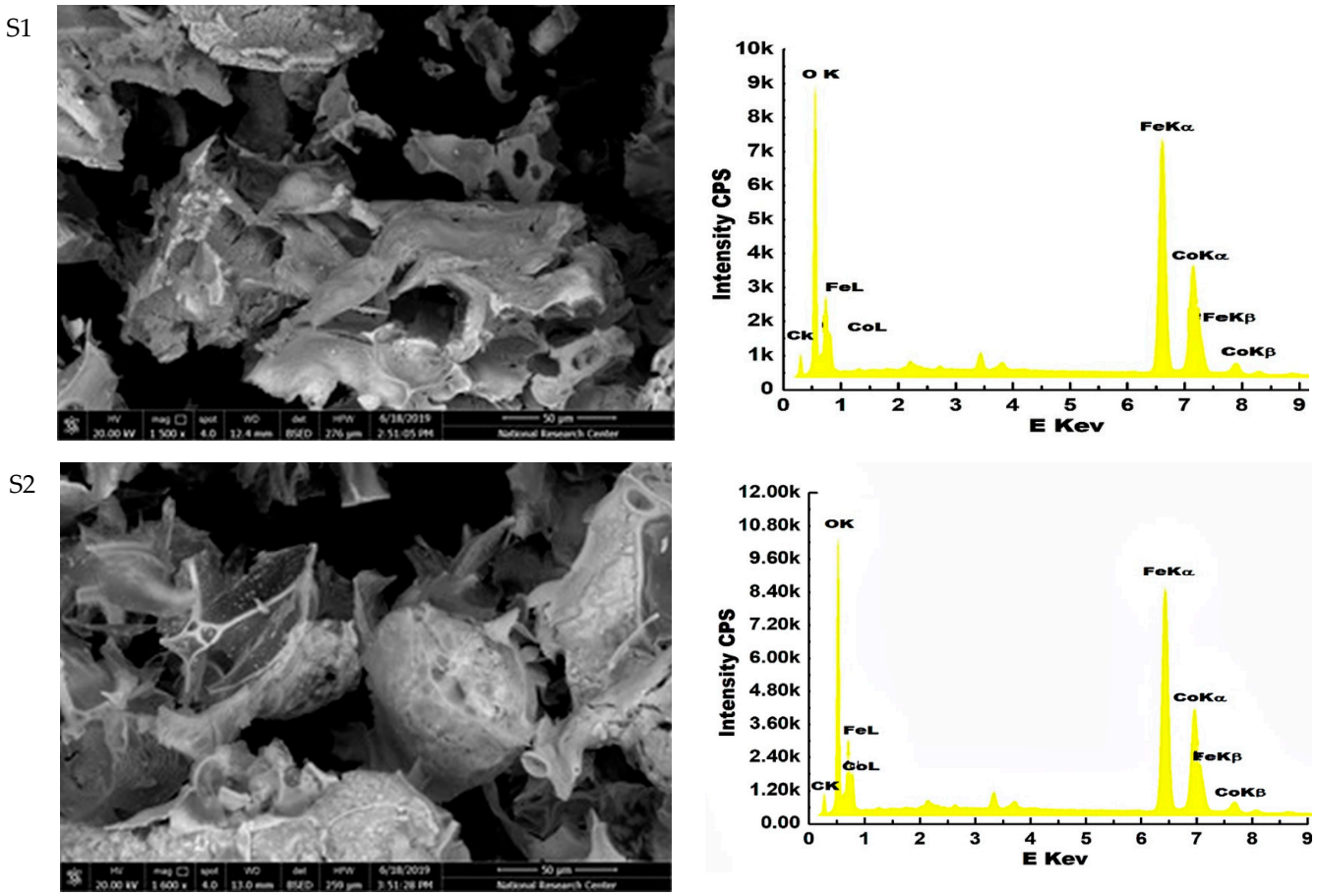


Figure 4. SEM and EDS of S1 and S2 solids.

In order for the surface morphology to be clearer, EDS analysis and EDS mapping were necessary. Here, Figure 4 also contains the EDS patterns of the S1 and S2 solids. These patterns prove the existence of the signal characteristic elements of copper (Cu), iron (Fe), and oxygen (O) in the S1 specimen. The same elements were observed in the patterns of S2 solid, with copper replaced by cobalt. Moreover, the observed signal at 0.27 Kev in the EDS patterns of S1 and S2 specimens is due to the presence of carbon (C) as an impurity; indeed, this finding is also confirmed in the obtained FTIR spectra. However, EDS mapping of the S1 and S2 samples indicate that Cu, Co, Fe, C, and O atoms are very well distributed, as shown in Figure 5.

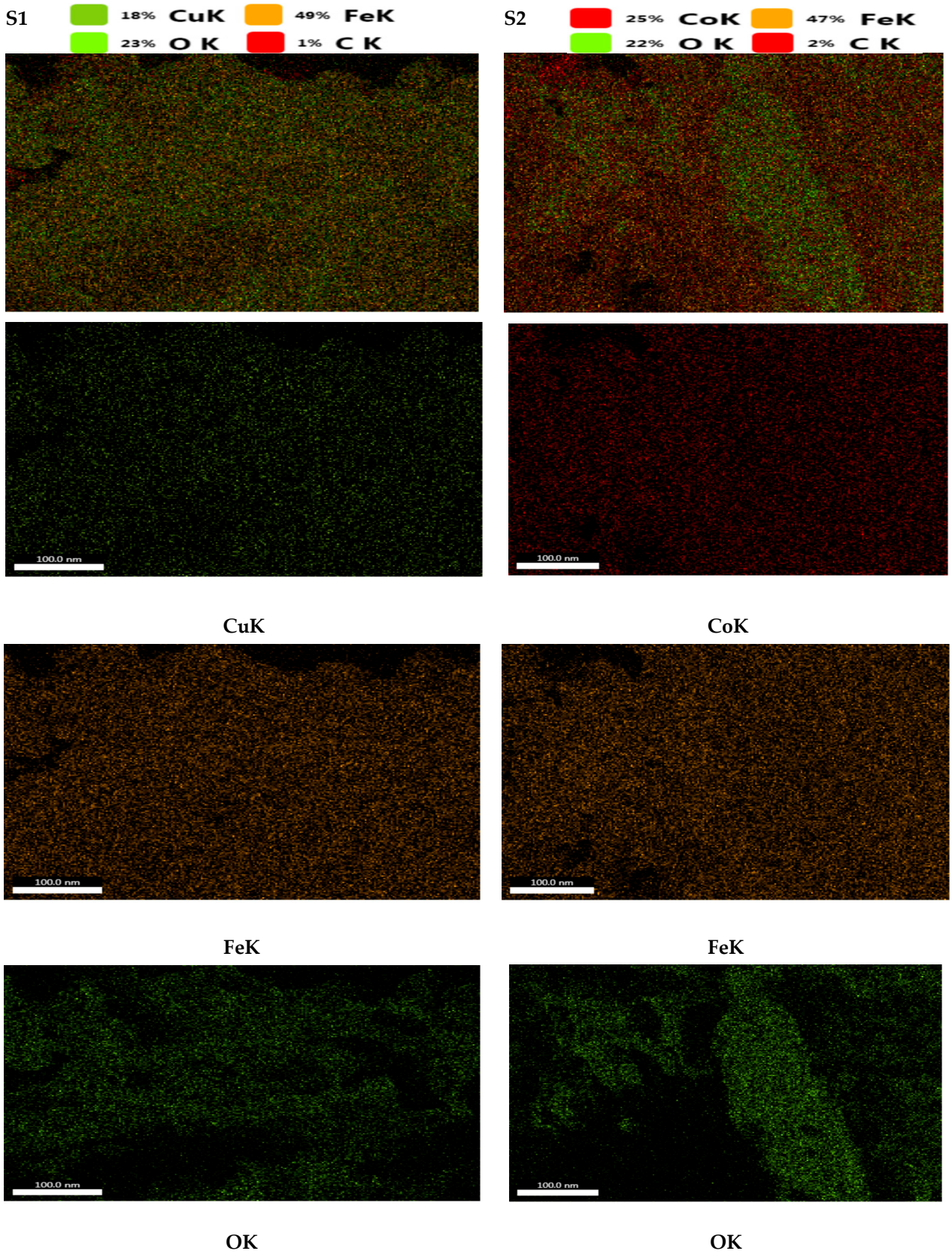
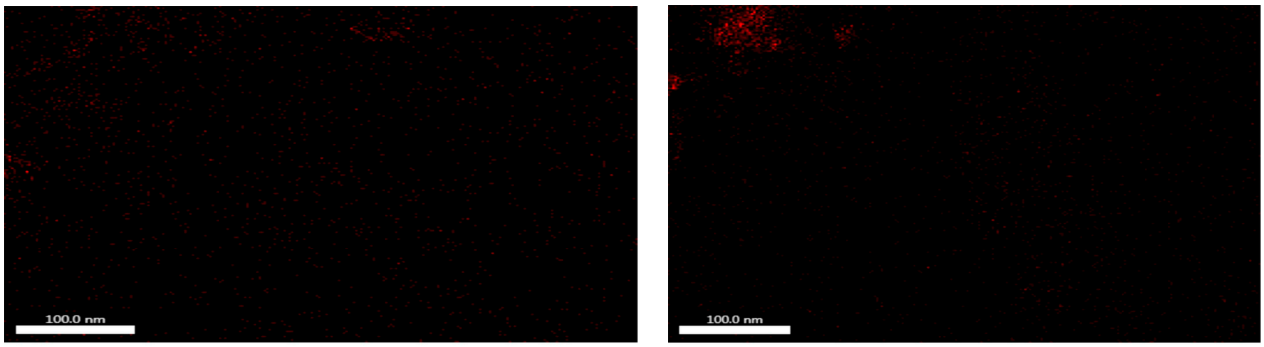


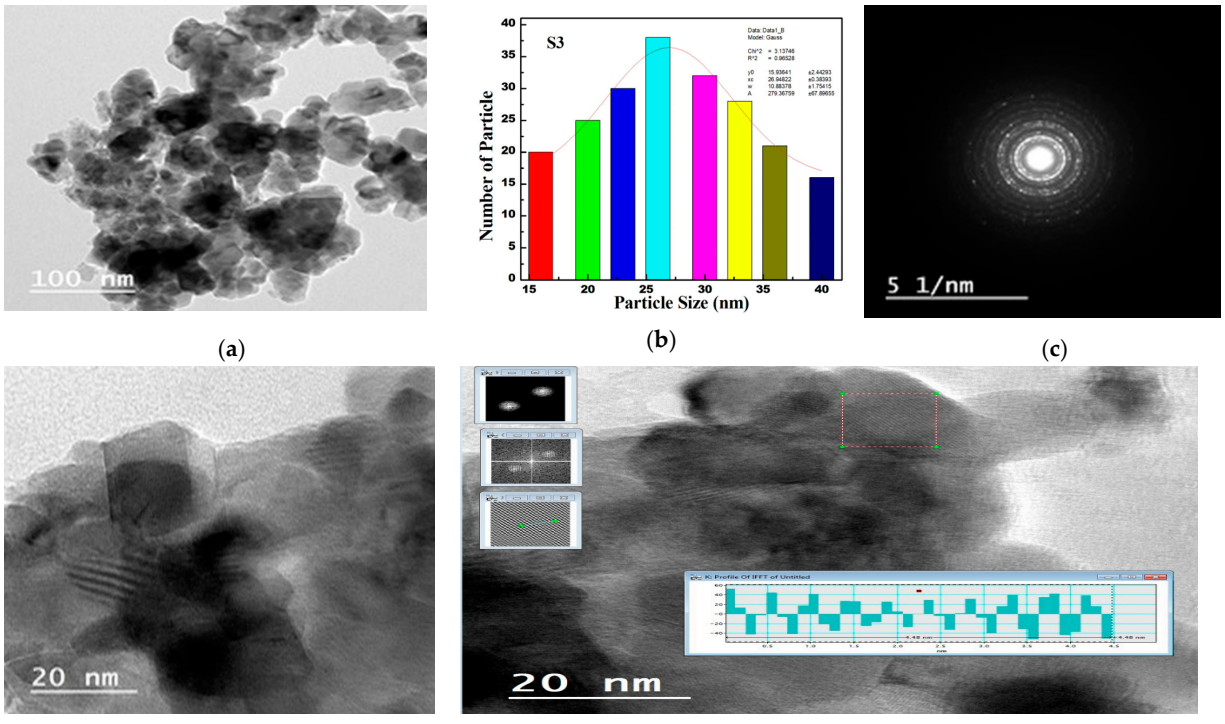
Figure 5. *Cont.*



CK **CK**

Figure 5. EDS Mapping of S1 and S2 solids.

Furthermore, because the S3 and S4 samples are calcined at 700 °C and have a good degree of crystallinity, as shown by the XRD analysis, we preferred to study their surface morphology using the TEM technique. TEM images of these specimens, their particle size histograms, fast Fourier transform (FFT) images, and continuously selected area electron diffraction (SAED) are included in Figures 6 and 7. The various TEM images demonstrated the effectiveness of the Corchorus olitorius dry leaf assisted combustion approach in producing both Cu and Co ferrites. Moreover, the ferrites' particles are homogeneous, uniform, and range in diameter from 25 nm to 60 nm. Fast Fourier transform (FFT) pictures showed a lattice fringe at 0.252 nm, which was related to the crystal plane of (311) and indicated a successful synthesis of cubic spinel copper and cobalt ferrites. On the other hand, the SAED analysis depicts little brilliant spots as varying-diameter rings surrounding a center area. The creation of polycrystalline Cu and Co ferrites was successful, as demonstrated by this finding.



(**a**) (**b**) (**c**)

(**d**)

Figure 6. TEM analysis of the S3 sample: (**a**) TEM; (**b**) particle size distribution; (**c**) SAED; and (**d**) FFT.

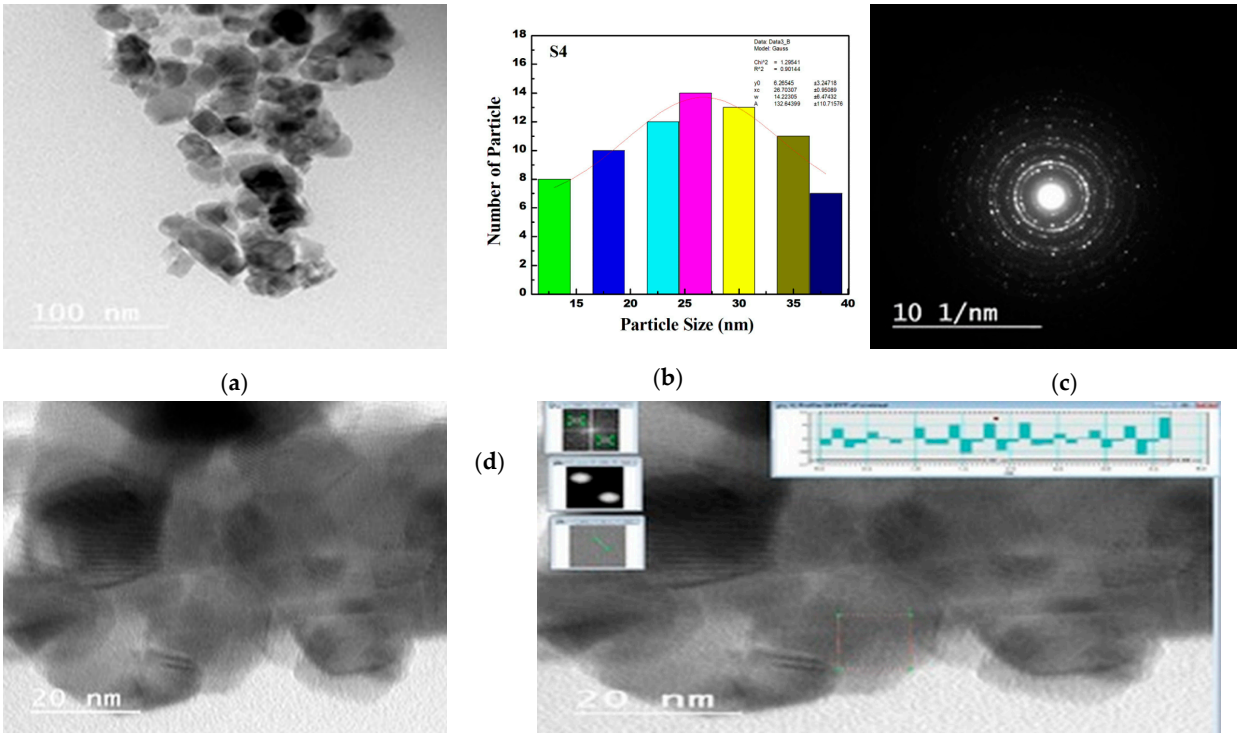


Figure 7. TEM analysis of the S4 sample: (**a**) TEM; (**b**) particle size distribution; (**c**) SAED; and (**d**) FFT.

3.5. Surface Properties

To determine the surface or textural properties, namely, S_{BET}, V_p, and r̂ for S1, S2, S3, and S4 solids, it was important to investigate the effects of calcination temperature and the used preparation method.

N_2 adsorption/desorption isotherms for these samples were detected at 77 K, as shown in Figure 8. These isotherms were used to elicit the surface characteristics for the as-synthesized samples. Table 3 contains the values of various surface parameters. These isotherms belong to type IV with H3-type hysteresis loop. After referring to Table 2, it was found that the calcination of the S2 sample at 700 °C led to a drop in the values of V_m and S_{BET}, while this treatment for the S1 sample resulted in an increase in these values. Opposite results are noted for the r̂ values of these specimens. Figure 7 displays the pore size distribution for the samples from S1 to S4 based on using Non-Local Density Functional Theory (NLDFT). Average pore sizes for the S1, S2, S3, and S4 samples are 9, 1, 1, and 10.5 nm, respectively.

S1

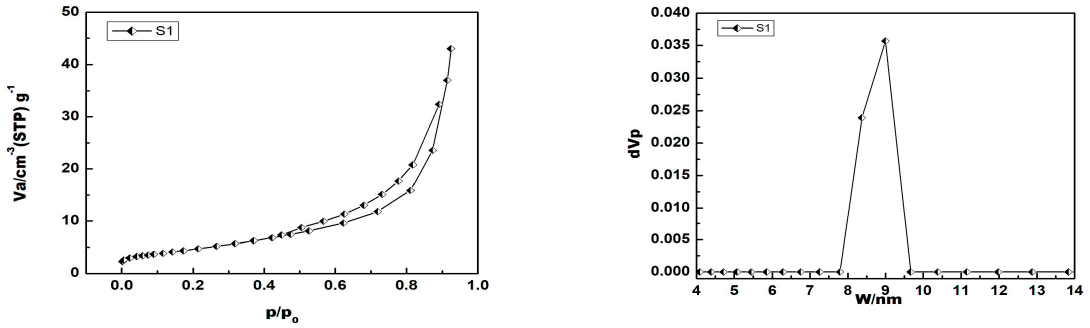


Figure 8. *Cont.*

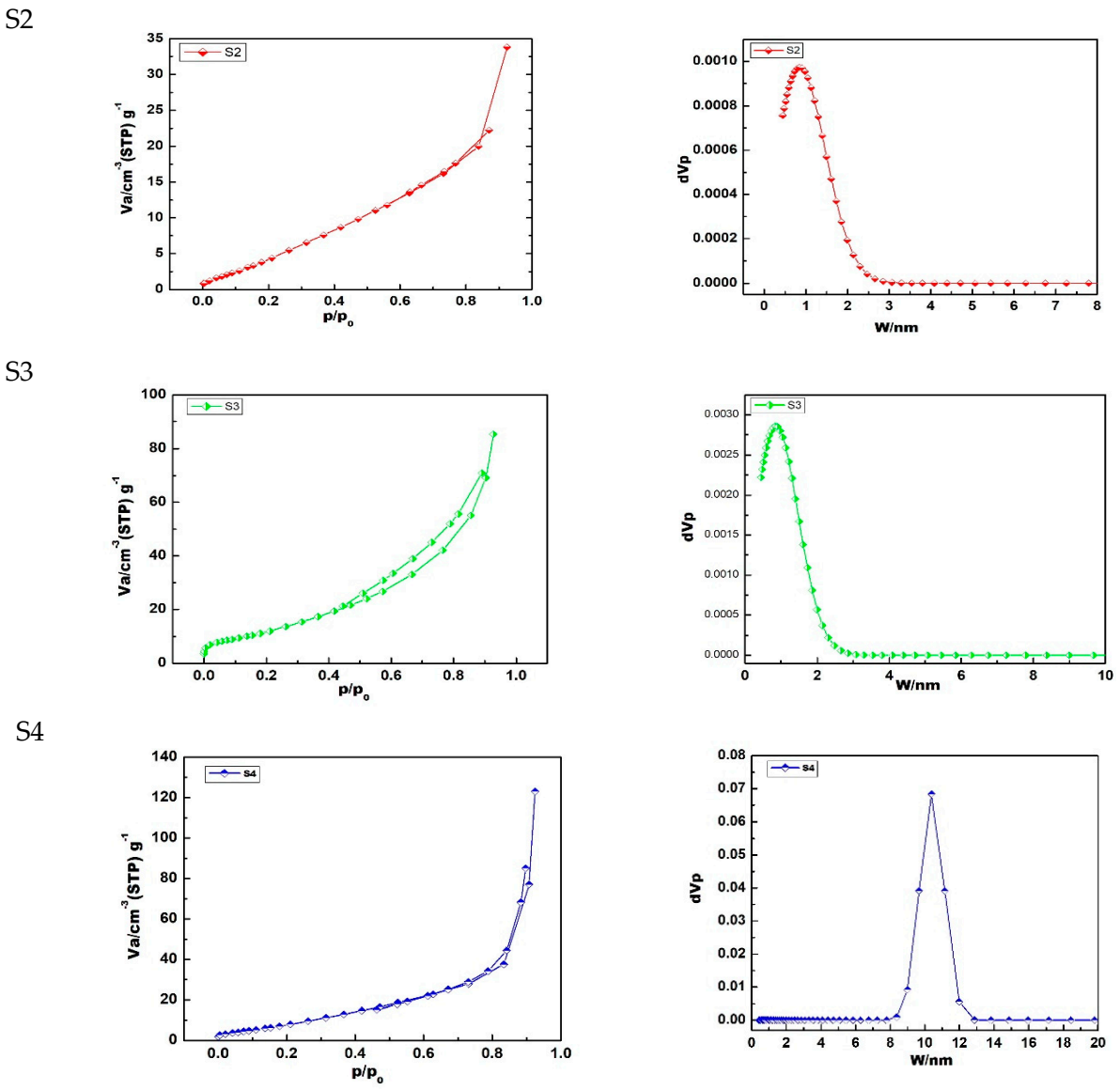


Figure 8. BET of S1, S2, S3, and S4 samples.

Table 3. Surface parameters of the S1, S2, S3, and S4 specimens.

Samples	S_{BET} (m^2/g)	V_m (cc/g)	V_p (cc/g)	$\hat{r}$ (nm)	BET-C (Constant)
S1	18	4.136	0.0665	14.78	31.38
S2	55	12.67	0.1319	9.57	10.85
S3	31.21	7.17	0.0523	6.704	3.54
S4	47.19	10.84	0.1903	16.134	5.21

3.6. Magnetic Behavior Study

The magnetic properties of the prepared samples were determined based on the hysteresis loops using VSM technique under applied magnetic field (±20 kG) at room temperature. Indeed, the magnetic properties involved different factors including the coercive field (H_c), remanent magnetization (M_r), and saturation magnetization (M_s). Moreover, these factors enabled us to calculate the squareness (Mr/Ms), anisotropy constant (K_a), and magnetic moment (μ_m) per unit formula in Bohr magnetrons. The magnetic parameters for the S3 and S4 specimens are noted in Table 4. These parameters have been

deduced from the magnetic curves and their hysteresis loop contained in Figure 9. In an overview of the results obtained, it was found that changing Cu to Co led to change in the values of all parameters. The values M_s, M_r, M_r/M_s, H_c, μ_m, and K_a for $CoFe_2O_4$ were higher than those of $CuFe_2O_4$.

Table 4. The magnetic properties of the S3 and S4 samples.

Samples	M_s (emu/g)	M_r (emu/g)	M_r/M_s (emu/g)	H_c (G)	μ_m	K_a (erg/cm^3)
S3	15.77	2.44	0.1547	154.03	0.6755	2479
S4	19.14	5.11	0.263	716.15	0.8047	13987

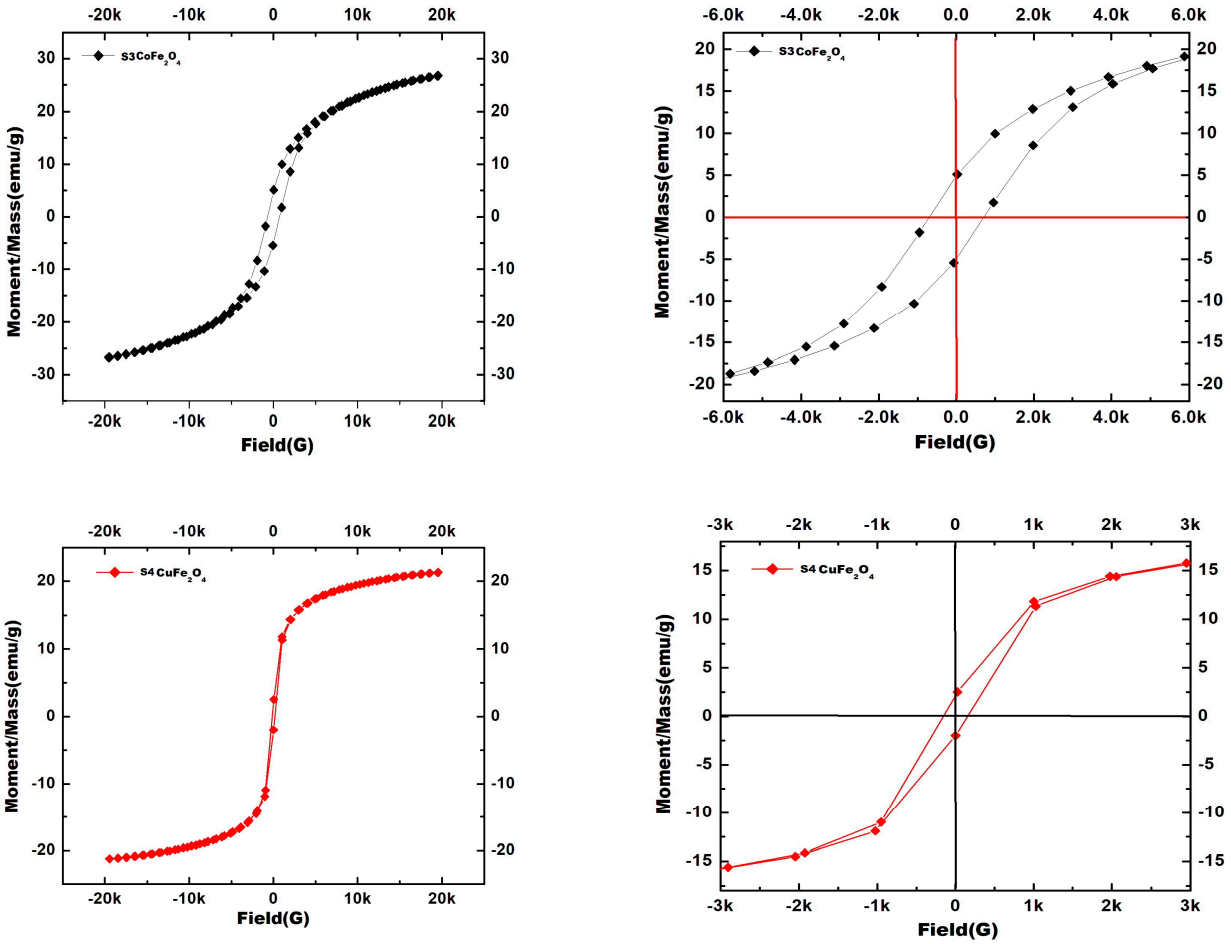


Figure 9. Magnetization curves for S3 and S4 samples.

4. Discussion

The S1 and S2 samples not containing dry leaves of Corchorus olitorius are non-crystalline based on preliminary XRD analysis. This strongly indicates the important and effective role of dry leaves of Corchorus olitorius in driving the solid–solid interaction between the interacting precursors to obtain Cu and Co ferrites. It also indicates the vital and effective role of the treatment of the investigated materials at 700 °C in catalyzing the reaction between them.

Fabrication of ferrites depends on the reaction in the solid–solid interaction between Fe oxides and another oxide of a divalent element. Among the iron ions that are present and should be present in the reaction medium is ferrous ion, which acts as a synergistic agent in driving such reactions, yielding the corresponding ferrites. [41]. This goal can be achieved by using fuel from natural products that provide us with a few carbon atoms as a

product of the combustion process. This small amount of carbon will reduce some of the ferric ions to ferrous ions, which act as synergistic agents [41].

The detailed mechanism of the solid–solid interaction between the stoichiometric oxides of either Cu or Co and Fe yielding either Cu or Co ferrites can be explained as follows [7,8,41]: (i) At the ferric oxide interface, two operations occur. The first operation involves the interaction between the divalent metal ions (M^{2+} = Cu^{2+} or Co^{2+}) and Fe_2O_3 yielding Fe^{2+} ions and the corresponding ferrite-based thin layer, which will surround Fe_2O_3 and impedes the progression of the solid–solid interaction between the interacting oxides. The second operation contains the reaction between some Fe_2O_3 and carbon resulting from the combustion of leaves of Corchorus olitorius yielding an additional amount of Fe^{2+} ions. (ii) Another reaction can be achieved between the resulting Fe^{2+} ions and the divalent metal oxide (MO) at its interface to produce an excess of the investigated ferrites with production of M^{2+} ions, which return to complete the solid–solid interaction and so on.

After returning to the X-ray analysis and examining it, the following was found: (i) The corresponding ferrites ($CuFe_2O_4$ and $CoFe_2O_4$) have been prepared successfully within the S1, S2, S3, and S4 specimens. (ii) The crystalitinity of the S1 and S2 solids is smaller than that of S3 and S4, respectively. (ii) All changes in the lattice parameters of $CuFe_2O_4$ and $CoFeFe_2O_4$ could be ascribed to the difference in the ionic radii of the reacting cations (Cu or Co) and their distribution. In this work, the IR and XRD measurements confirmed the success of the combustion method based on the dry leaves of Corchorus olitorius in preparation of the ferrites studied. These analyses show a slight shift and enhanced crystallinity in X-ray diffractograms of Cu and Co ferrites by heating at 700 °C, with the emergence of two fundamental (FTIR) vibration modes related to spinel-type ferrite. IR spectra show that the S1 and S2 samples contain trace amounts of carbon, which stimulate the solid–solid interaction, especially at 700 °C, yielding Cu and Co ferrites. At 700 °C, the carbon atoms disappear from the S3 and S4 samples after catalyzing the previous reaction, and the evidence for this disappearance is the absence of the vibration band located at 1356–1348 cm^{-1}. XRD, SEM, EDS, TEM, FFT, and SAED analyses confirm fabrication of polycrystalline particles having size ranging between 17 nm and 60 nm.

Varios isotherms for the fabricated materials show complex pore structures. These isotherms show adsorption processes on the surface of each sample, with pores of differing widths due to the difference in pore shape(s). Different features typically associated with micro-/mesoporous characteristics were observed in the specimens studied. At low pressures, micro-pores filling led to a sharp rise in the adsorption section. At elevated pressure range, capillary condensation inside meso-pores occurred due to multilayer adsorption. Delayed pore condensation can be achieved in the voids between the particles as shown in the S2 and S4 solids depending on the presence of networking effects such as pore blocking, cavitation, and metastability of the adsorbed multilayer. Moreover, the capillary condensation process is accompanied by an apparent type-H3 hysteresis. The different shapes of this hysteresis are also related to non-rigid aggregates of plate-like particles, which are slit-like pores. The desorption section is parallel to the adsorption section, with formation of a narrow hysteresis loop. This section is parallel to the adsorption section. These results confirm the presence of limited networking effects with a narrow distribution of uniform meso-pores. Pore size distribution patterns of different solids display one model at the micro/meso-pore scale. The values of average pore size of the S1 and S2 specimens are 9 nm and 1 nm, while the values of the S2 and S4 solids are 14.78 nm and 6.70 nm, respectively. This indicates pore narrowing with subsequent increase in the surface area of the S3 solid. Opposite findings were observed with the S4 specimen.

Studying the hysteresis cycle resulting from applying a magnetic field to the S3 and S4 samples led to the determination of their magnetic properties. The hysteresis loops show the soft and hard magnetic behaviors typical for $CuFe_2O_4$ and $CoFe_2O_4$ nanoparticles, respectively. The most important factor affecting the magnetic behavior of the Cu and Co ferrites studied is the cation distribution at A- and B-sites of their spinel structures. The

ionic radii, crystal lattice, fabrication method, and heat treatment all had clear effects on the distribution of Fe, Cu, and Co ions and the magnetic characteristics of the Cu and Co ferrites studied [41].

The magnetism for the S4 solid is higher than that of the S3 solid. The replacement of Cu cations by Co cations led to enhancing the magnetization depending on the surface spin disorder, although these cations have the same magnetic moment [42]. The origin of the interactions between the different cations at A- and B-sublattices in the spinel Cu or Co ferrites consists of three sections as follows: (i) the intersublattice (A–B) super-exchange interactions, which are much stronger that other interactions; (ii) the intrasublattice (A–A and B–B) exchange interactions [43]. (iii) The transition of some Fe^{3+} ions from A-site to B-site due to migration of some Cu or Co ions from B-site to A-site led to stimulating the super-exchange interactions of $Fe_A{}^{3+}$–$Fe_B{}^{3+}$ ions [7,8]. This result is more pronounced in case of $CoFe_2O_4$ compared to $CuFe_2O_4$ nanoparticles. This behavior is due to nature, orientation, and concentrations of Co and Cu cations in A- and B-sites. These findings resulted in enhancement in the intersublattice (A–B) super-exchange interactions compared with the intrasublattice (A–A) and (B–B) exchange interactions [42,43]. Another factor that can be included among the reasons for the high magnetism of cobalt ferrite is the large size of its grains compared to copper ferrite.

The as-synthesized ferrites have multiple domain types depending on the drop in their squareness [41]. Because the squareness and coercivity can be also linked to the magnetic anisotropy and super-exchange interaction between the cations in A- and B-sites, $CoFe_2O_4$ has a higher anisotropy constant (13987 erg/cm^3) compared to $CuFe_2O_4$ (2479 erg/cm^3).

Finally, a comparison can be made between the structural properties and the magnetic behavior of the as-synthesized cobalt and copper ferrites and that reported in literature. This comparison concluded that the results of magnetic behavior in our study are consistent with many investigations and at the same time are inferior to the typical Co and Cu ferrites [44–49]. Similar results to those of our study show that the M_s value calculated for nanosized cobalt ferrite fabricated by sol-gel method is lower than that for the bulk samples, which is a consequence of the superparamagnetic nature of the magnetic nanoparticles [47,48]. These results are attributed by the authors to surface defects and morphology. The authors of these studies added that the surface defects are due to finite-size scaling of nanocrystallites, which in turn leads to a non-collinearity of magnetic moments on their surface with an increase in their coercivity. They confirm that these effects are more intense in a ferromagnetic system, where the super-exchange interaction occurs through the oxygen ion, O^{2-} [49]. The high magnetocrystalline anisotropy of $CoFe_2O_4$ arises from the Co^{2+} ions that are present at B-site (octahedral site) in inverse spinel structure [46]. Thus, a change in the preparation-method-dependent cation distribution leads to changes in the magnetism, magnetocrystalline anisotropy, and magnetic coercivity. Moreover, the lattice constant (a) of the as-prepared Co ferrite is about 0.8366 nm, consistent with the range of the results in the literature, which resulted in lower X-ray density [45,50]. On the other hand, the co-precipitation method assisted by microwave with octanoic acid resulted in fabrication of $CuFe_2O_4$ nanoparticles with particle size of 20 nm [51]. The resulting Cu ferrite exhibited a weak ferromagnetic behavior with the H_c value of 133.50 G, the M_s value of 32.43 emu/g, and the M_r value of 2.68 emu/g. which was comparable to the M_s values of 39 emu/g and 30 emu/g for $CuFe_2O_4$ with 50 nm and 10-20 nm, respectively. These results confirm that the magnetization of $CuFe_2O_4$ nanoparticles is strongly dependent on their particle size [52,53].

5. Conclusions

This manuscript has proven to us the success of the self-combustion method assisted by dry leaves of Corchorus olitorius in preparing nanosized Cu and Co ferrite particles. From this study, the following important points can be drawn:

1. The preparation method used is important because it is economical in terms of its reliance on an available natural product. A glowing self-combustion resulted in the nucleation and crystallization of copper and cobalt ferrite particles.
2. The heat treatment at 700 °C led to enhancing the crystallinity of Co and Cu ferrites nanoparticles with different modifications to the most structural properties of these ferrites. The thermal analysis confirms formation of chemically stable Co and Cu ferrites.
3. The as-prepared Cu and Co ferrites have spinel-type structure with two characteristic vibration bands around 400 cm^{-1} and 600 cm^{-1}.
4. The calcination at 700 °C resulted in a drop in the values of S_{BET} and V_m for Co ferrite with an increase in these values of Cu ferrite and change in the material's pore structure.
5. The magnetisms of $CuFe_2O_4$ and $CoFe_2O_4$ are 15.77 emu/g and 19.14 emu/g, respectively.

Author Contributions: Conceptualization, N.M.D. and O.H.A.-E.; methodology, N.S.A.-K.; software, O.H.A.-E.; validation, G.M.A.-S., R.S.A. and N.S.A.-K.; formal analysis, O.H.A.-E.; investigation, N.M.D.; resources, N.S.A.-K.; data curation, O.H.A.-E.; writing—original draft preparation, N.M.D. and O.H.A.-E.; writing—review and editing, N.M.D. and O.H.A.-E.; visualization, O.H.A.-E.; supervision, N.M.D.; project administration, N.S.A.-K.; funding acquisition, N.S.A.-K., G.M.A.-S. and R.S.A. All authors have read and agreed to the published version of the manuscript.

Funding: This research was funded by the Princess Nourah bint Abdulrahman University Researchers Supporting Project number (PNURSP2023R85), Princess Nourah bint Abdulrahman University, Riyadh, Saudi Arabia.

Data Availability Statement: The data presented in this study are available on request from the corresponding author.

Acknowledgments: The authors would like to extend their sincere appreciation to the Princess Nourah bint Abdulrahman University Researchers Supporting Project number (PNURSP2023R85), Princess Nourah bint Abdulrahman University, Riyadh, Saudi Arabia.

Conflicts of Interest: The authors declare no conflict of interest.

References

1. Ye, Z.; Deng, Z.; Zhang, L.; Chen, J.; Wang, G.; Wu, Z. The structure of copper ferrite prepared by five methods and its catalytic activity on lignin oxidative degradation. *Mater. Res. Express* **2020**, *7*, 035007.
2. Wang, L.; Bock, D.C.; Li, J.; Stach, E.A.; Marschilok, A.C.; Takeuchi, K.J.; Takeuchi, E.S. Synthesis and Characterization of $CuFe_2O_4$ Nano/sub-micron Wires-Carbon Nanotube Composites as Binder-free Anodes for Li-ion Batteries. *ACS Appl. Mater. Interfaces* **2018**, *10*, 8770–8785. [CrossRef] [PubMed]
3. Tamboli, Q.Y.; Patange, S.M.; Mohanta, Y.K.; Sharma, R.; Zakde, K.R. Synthesis of Cobalt Ferrite Nanoparticles: An Emerging Material for Environmental and Biomedical Applications. *J. Nanomater.* **2023**, *2023*, 9770212. [CrossRef]
4. Lassoued, A.; Ben Hassine, M.; Karolak, F.; Dkhil, B.; Ammar, S.; Gadri, A. Synthesis and magnetic characterization of Spinel ferrites MFe_2O_4 (M = Ni, Co, Zn and Cu) via chemical co-precipitation method. *J. Mater. Sci. Mater. Electron.* **2017**, *28*, 18857–18864. [CrossRef]
5. Xian, G.; Kong, S.; Li, Q.; Zhang, G.; Zhou, N.; Du, H.; Niu, L. Synthesis of Spinel Ferrite MFe_2O_4 (M = Co, Cu, Mn, and Zn) for Persulfate Activation to Remove Aqueous Organics: Effects of M-Site Metal and Synthetic Method. *Front. Chem.* **2020**, *8*, 177. [CrossRef]
6. Al-Senani, G.M.; Al-Fawzan, F.F.; Almufarij, R.S.; Abd-Elkader, O.H.; Deraz, N.M. Magnetic Behavior of Virgin and Lithiated $NiFe_2O_4$ Nanoparticles. *Crystals* **2023**, *13*, 69. [CrossRef]
7. Deraz, N.M. Size and crystallinity-dependent magnetic properties of copper ferrite nano-particles. *J. Alloy. Compd.* **2010**, *501*, 317–325. [CrossRef]
8. Deraz, N.M. Glycine-assisted fabrication of nanocrystalline cobalt ferrite system. *J. Anal. Appl. Pyrolysis* **2010**, *88*, 103–109. [CrossRef]
9. Chagas, E.F.; Ponce, A.S.; Prado, R.J.; Silva, G.M.; Bettini, J. Thermal effect on magnetic parameters of high-coercivity cobalt ferrite. *J. Appl. Phys.* **2014**, *116*, 033901. [CrossRef]
10. Galizia, P.; Cernea, M.; Mihalache, V.; Diamandescu, L.; Maizza, G.; Galassi, C. Easy batch-scale production of cobalt ferrite nanopowders by two-step milling: Structural and magnetic characterization. *Mater. Des.* **2017**, *130*, 327–335. [CrossRef]

11. Tomiczek, A.E. Effect of milling time on microstructure of cobalt ferrites synthesized by mechanical alloying. *Arch. Mater. Sci. Eng.* **2021**, *111*, 1. [CrossRef]
12. Shemer, G.; Tirosh, E.; Livneh, T.; Markovich, G. Tuning a colloidal synthesis to control CO^2+ doping in ferrite nanocrystals. *J. Phys. Chem. C* **2007**, *111*, 14334–14338. [CrossRef]
13. Sharma, S.; Sharma, N.D.; Choudhary, N.; Verma, M.K.; Singh, D. Chromium incorporated nanocrystalline cobalt ferrite synthesized by combustion method: Effect of fuel and temperature. *Ceram. Int.* **2017**, *43*, 13401–13410. [CrossRef]
14. Deshmukh, S.S.; Humbe, A.V.; Kumar, A.; Dorik, R.G.; Jadhav, K.M. Urea assisted synthesis of $Ni_{1-X}Zn_xFe_2O_4$($0 \leq x \leq 0.8$): Magnetic and Mössbauer investigations. *J. Alloy. Compd.* **2017**, *704*, 227–236. [CrossRef]
15. Ali, M.B.; El Maalam, K.; El Moussaoui, H.; Mounkachi, O.; Hamedoun, M.; Masrour, R.; Hlil, E.K.; Benyoussef, A. Effect of zinc concentration on the structural and magnetic properties of mixed Co–Zn ferrites nanoparticles synthesized by sol/gel method. *J. Magn. Magn. Mater.* **2016**, *398*, 20–25.
16. Deraz, N.M. Facile and eco-friendly route for green synthesis of magnesium ferrite nano particles. *Sci. Sinter.* **2020**, *52*, 53–65. [CrossRef]
17. Gul, S.; Khan, S.B.; Rehman, I.U.; Khan, M.A.; Khan, M.I. A comprehensive review of magnetic nanomaterials modern day theranostics. *Front. Mater.* **2019**, *6*, 179. [CrossRef]
18. Deraz, N.M. Incandescent Combustion Synthesis of Nanomagnetic Ni/NiO Composites. *Sci. Sinter.* **2021**, *53*, 155–167. [CrossRef]
19. Franco, A.; Machado, F.L.A.; Zapf, V.S. Magnetic properties of nanoparticles of cobalt ferrite at high magnetic field. *J. Appl. Phys.* **2011**, *110*, 053913. [CrossRef]
20. Ghaani, M.; Saffari, J. Synthesis of $CuFe_2O_4$ Nanoparticles by a new co-precipitation method and using them as Efficient Catalyst for One-pot Synthesis of Naphthoxazinones. *J. Nanostruct.* **2016**, *6*, 172–178.
21. Song, Q.; Zhang, Z.J. Controlled synthesis and magnetic properties of bimagnetic spinel ferrite $CoFe_2O_4$ and $MnFe_2O_4$ nanocrystals with core–shell architecture. *J. Am. Chem. Soc.* **2012**, *134*, 10182–10190. [CrossRef]
22. Gurgel, A.L.; Martinelli, A.E.; de Aquino Conceição, O.L.; Xavier, M.M., Jr.; Torres, M.A.M.; de Araújo Melo, D.M. Microwave-assisted hydrothermal synthesis and magnetic properties of nanostructured cobalt ferrite. *J. Alloy. Compd.* **2019**, *799*, 36–42. [CrossRef]
23. Kumar, V.; Rana, A.; Yadav, M.S.; Pant, R.P. Size-induced effect on nano-crystalline $CoFe_2O_4$. *J. Magn. Magn. Mater.* **2008**, *302*, 1729–1734. [CrossRef]
24. Mahdikhah, V.; Ataie, A.; Babaei, A.; Sheibani, S.; Ow-Yang, C.W.; Abkenar, S.K. Control of structural and magnetic characteristics of cobalt ferrite by post-calcination mechanical milling. *J. Phys. Chem. Solids* **2019**, *134*, 286–294.
25. Liu, B.L.; Fu, Y.P.; Wang, M.L. Magnetic and catalytic properties of copper ferrite nanopowders prepared by combustion process. *J. Nanosci. Nanotechnol.* **2009**, *9*, 1491–1495. [CrossRef] [PubMed]
26. Kuznetsov, M.V.; Morozov, Y.G.; Belousova, O.V. Synthesis of Copper Ferrite Nanoparticles. *Inorg. Mater.* **2013**, *49*, 606–615. [CrossRef]
27. Ayesh, A.I.; Abu Haija, M.; Shaheen, A.; Banat, F. Spinel ferrite nanoparticles for H_2S gas sensor. *Appl. Phys. A* **2017**, *123*, 682. [CrossRef]
28. Alves, T.E.P.; Pessoni, H.V.S.; Franco, A., Jr. The effect of Y^{3+} substitution on the structural, optical band-gap, and magnetic properties of cobalt ferrite nanoparticles. *Phys. Chem. Chem. Phys.* **2017**, *19*, 16395–16405. [CrossRef]
29. Abdellatif, M.H.; Innocenti, C.; Liakos, I.; Scarpellini, A.; Marras, S.; Salerno, M. Effect of Jahn-Teller distortion on the short range magnetic order in copper ferrite. *J. Magn. Magn. Mater.* **2017**, *424*, 402–409.
30. Haija, M.A.; Abu-Hani, A.F.; Hamdan, N.; Stephen, S.; Ayesh, A.I. Characterization of H_2S gas sensor based on $CuFe_2O_4$ nanoparticles. *J. Alloy. Compd.* **2017**, *690*, 461–468. [CrossRef]
31. Zhuravlev, V.A.; Minin, R.V.; Itin, V.I.; Lilenko, I.Y. Structural parameters and magnetic properties of copper ferrite nanopowders obtained by the sol-gel combustion. *J. Alloy. Compd.* **2017**, *692*, 705–712. [CrossRef]
32. Le Trong, H.; Presmanes, L.; De Grave, E.; Barnabé, A.; Bonningue, C.; Tailhades, P. Mössbauer characterisations and magnetic properties of iron cobaltites $Co_xFe_{3-x}O_4$ ($1 \leq x \leq 2.46$) before and after spinodal decomposition. *J. Magn. Magn. Mater.* **2013**, *334*, 66–73. [CrossRef]
33. Sawatzky, G.A.; Van Der Woude, F.; Morrish, A.H. Cation distributions in octahedral and tetrahedral sites of the ferrimagnetic spinel $CoFe_2O_4$. *J. Appl. Phys.* **1968**, *39*, 1204–1205. [CrossRef]
34. Blanco-Gutiérrez, V.; Gallastegui, J.A.; Bonville, P.; Torralvo-Fernandez, M.J.; Sáez-Puche, R. MFe_2O_4 (M: Co^{2+}, Ni^{2+}) Nanoparticles: Mossbauer and X-ray Absorption Spectroscopies Studies and High-Temperature Superparamagnetic Behavior. *J. Phys. Chem. C* **2012**, *116*, 24331–24339. [CrossRef]
35. Peddis, D.; Yaacoub, N.; Ferretti, M.; Martinelli, A.; Piccaluga, G.; Musinu, A.N.N.A.; Cannas, C.; Navarra, G.; Greneche, J.M.; Fiorani, D. Cationic distribution and spin canting in $CoFe_2O_4$ nanoparticles. *J. Phys. Condens. Matter* **2011**, *23*, 426004. [CrossRef]
36. Mameli, V.; Musinu, A.; Ardu, A.; Ennas, G.; Peddis, D.; Niznansky, D.; Sangregorio, C.; Innocenti, C.; Thanh, N.T.; Cannas, C. Studying the effect of Zn-substitution on the magnetic and hyperthermic properties of cobalt ferrite nanoparticles. *Nanoscale* **2016**, *8*, 10124–10137. [CrossRef] [PubMed]
37. Abd-Elkader, O.H.; Al-Enizi, A.M.; Shaikh, S.F.; Ubaidullah, M.; Abdelkader, M.O.; Mostafa, N.Y. Enhancing the Liquefied Petroleum Gas Sensing Sensitivity of Mn-Ferrite with VanadiumDoping. *Processes* **2022**, *10*, 2012. [CrossRef]
38. Waldron, R.D. Infrared spectra of ferrites. *Phys. Rev.* **1955**, *99*, 1727–1735. [CrossRef]

39. Al-Senani, G.M.; Al-Fawzan, F.F.; Almufarij, R.S.; Abd-Elkader, O.H.; Deraz, N.M. Biosynthesis, Physicochemical and Magnetic Properties of Inverse Spinel Nickel Ferrite System. *Crystals* **2022**, *12*, 1542. [CrossRef]
40. Al-Enizi, A.M.; Abd-Elkader, O.H.; Shaikh, S.F.; Ubaidullah, M.; Abdelkader, M.O.; Mostafa, N.Y. Fabrication and Characterization of W-Substituted $ZnFe_2O_4$ for Gas Sensing Applications. *Coatings* **2022**, *12*, 1355. [CrossRef]
41. Abd-Elkader, O.; Al-Enizi, A.M.; Shaikh, S.F.; Ubaidullah, M.; Abdelkader, M.O.; Mostafa, N.Y. The Structure, Magnetic, and Gas Sensing Characteristics of W-Substituted Co-Ferrite Nanoparticles. *Crystals* **2022**, *12*, 393. [CrossRef]
42. Gu, Z.; Xiang, X.; Fan, G.; Li, F. Facile synthesis and characterization of cobalt ferrite nanocrystals via a simple reduction−oxidation route. *J. Phys. Chem. C* **2008**, *112*, 18459–18466. [CrossRef]
43. Ammar, S.; Jouini, N.; Fiévet, F.; Beji, Z.; Smiri, L.; Moliné, P.; Danot, M.; Grenèche, J.M. Magnetic properties of zinc ferrite nanoparticles synthesized by hydrolysis in a polyol medium. *J. Phys. Condens. Matter* **2006**, *18*, 9055. [CrossRef]
44. Kodama, R.H.; Berkowitz, A.E.; McNiff, E.J., Jr.; Foner, S. Surface spin disorder in ferrite nanoparticles. *J. Appl. Phys.* **1997**, *81*, 5552–5557. [CrossRef]
45. Sharifi, A.; Hayati, R.; Setoudeh, N.; Rezaei, G. A comparison between structural and magnetic behavior of cobalt ferrite synthesized via solid state and chemical methods. *Mater. Res. Express* **2021**, *8*, 106103. [CrossRef]
46. Limaye, M.V.; Singh, S.B.; Date, S.K.; Kothari, D.; Reddy, V.R.; Gupta, A.; Sathe, V.; Choudhary, R.J.; Kulkarni, S.K. High coercivity of oleic acid capped $CoFe_2O_4$ nanoparticles at room temperature. *J. Phys. Chem. B* **2009**, *113*, 9070–9076. [CrossRef] [PubMed]
47. Houshiar, M.; Zebhi, F.; Razi, Z.J.; Alidoust, A.; Askari, Z. Synthesis of cobalt ferrite ($CoFe_2O_4$) nanoparticles using combustion, coprecipitation, and precipitation methods: A comparison study of size, structural, and magnetic properties. *J. Magn. Magn. Mater.* **2014**, *371*, 43–48. [CrossRef]
48. Fotukian, S.M.; Barati, A.; Soleymani, M.; Alizadeh, A.M. Solvothermal synthesis of $CuFe_2O_4$ and Fe_3O_4 nanoparticles with high heating efficiency for magnetic hyperthermia application. *J. Alloy. Compd.* **2020**, *816*, 152548. [CrossRef]
49. Hien, N.T.; Truong, N.X.; Oanh, V.T.K.; Hai, P.V.; Ca, N.X.; Van, H.T.; Vuong, N.V. Preparation of exchange coupled $CoFe_2O_4/CoFe_2$ nanopowders. *J. Magn. Magn. Mater.* **2020**, *511*, 166984. [CrossRef]
50. Salunkhe, A.B.; Khot, V.M.; Phadatare, M.R.; Pawar, S.H. Combustion synthesis of cobalt ferrite nanoparticles—Influence of fuel to oxidizer ratio. *J. Alloy. Compd.* **2012**, *514*, 91–96. [CrossRef]
51. Abd-Elkader, H.O.; Deraz, N.M. Synthesis and Characterization of New Copper based Nanocomposite. *Int. J. Electrochem. Sci.* **2013**, *8*, 8614–8622.
52. Deng, H.; Chen, H.; Li, H. Synthesis of crystal MFe_2O_4 (M = Mg, Cu, Ni) microspheres. *Mater. Chem. Phys.* **2007**, *101*, 509–551. [CrossRef]
53. Farghali, A.A.; Khedr, M.H.; Khalek, A.A.A. Catalytic decomposition of carbondioxide over freshly reduced activated $CuFe_2O_4$ nano-crystals. *J. Mater. Process. Technol.* **2007**, *181*, 81–87. [CrossRef]

Disclaimer/Publisher's Note: The statements, opinions and data contained in all publications are solely those of the individual author(s) and contributor(s) and not of MDPI and/or the editor(s). MDPI and/or the editor(s) disclaim responsibility for any injury to people or property resulting from any ideas, methods, instructions or products referred to in the content.